Chapter 7: Transcritical flow

7.1. Introduction

Transcritical flows over mobile beds are challenging to model due to the rapid variation in sediment transport with space and time and due to the specific treatment required for boundary conditions. The two-layer and the Saint-Venant – Exner models are confronted with the experimental data of two kinds of transcritical flow: (1) a control section over a changing slope (Bellal et al., 2004) and (2) a hydraulic jump over a mobile bed (Bellal et al., 2003). For each of these cases, a short description of the physical phenomenon and the experimental process is given. Then, the calibration of the friction coefficients and the way to handle the boundary conditions are exposed for the common (Saint-Venant – Exner) and the two-layer approaches. Afterwards, the water and bed profiles, computed with both numerical models, are compared together and with measurements. A part of these results is exposed in Savary et al. (2006) and Savary and Zech (2007).

7.2. Knickpoint migration

7.2.1. Physical description

The experiment carried out by Mourad Bellal (Bellal et al. 2004) illustrates the morphological changes due to a transition from a mild to a steep bed slope. The knickpoint represents the point of abrupt change in the longitudinal bottom profile of the channel. The flow regime, which is subcritical over the mild slope (water profile M_2) becomes supercritical over the steep slope (water profile S_2) (Fig. 7.1). A control section thus corresponds to the knickpoint. The time-evolution of the bed and water profiles is illustrated on Figure 7.1. As initially described by Brush and

Wolman (1960), the knickpoint is associated with an important increase in bed shear stress and in transport rate. The knickpoint and the control section propagate upstream due to regressive erosion. As a result, the slope in the supercritical reach flattens and the slope variation between the upstream and downstream slopes dies down. The toe of the steep slope, corresponding to the downstream end of the channel, is non erodible. Thus, its level remains the same during the regressive erosion.

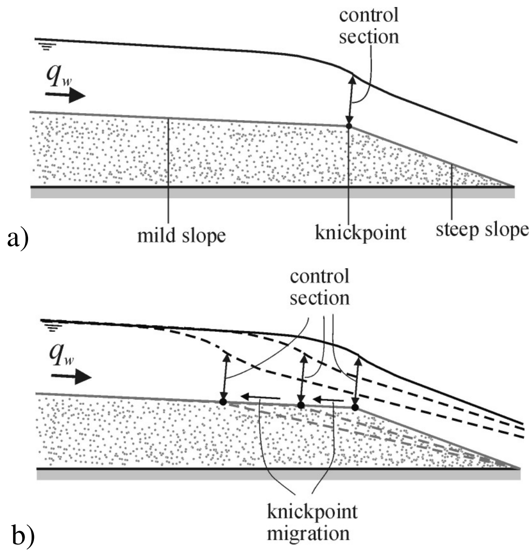

Figure 7.1. (a) Initial condition (b) Knickpoint migration (inspired from Bellal et al, 2004)

In initial conditions, the knickpoint is pre-formed and is located at 1 m (Table 7.1, run 1-3) or 1.1 m (Table 1, run 4-5) from the downstream end of the flume. The sediment bed is saturated with a small liquid discharge. Afterwards, the liquid discharge is progressively increased up to the experimental value. There is no sediment supply upstream. At the end of the experiment, the control section and the knickpoint vanish as a subcritical flow takes place. As there is no sediment supply, no equilibrium state is reached. Several experiments were performed with the initial parameters presented in Table 7.1.

Test #	Q (l/s)	S_0^{up} %	S_0^{dwn} %
Run 1	4.90	0.4	2.02
Run 2	6.15	0.47	2.03
Run 3	7.33	0.45	2.00
Run 4	5.01	0.42	3.02
Run 5	6.18	0.44	5.03

Table 7.1. Experimental data (Bellal et al., 2004)

The water and the bed levels were measured respectively by the ultrasonic probe and by the bed profiler (detailed in chapter 5). The two models have been applied to the experiment presented as Run 1 in Table 7.1 meaning the liquid discharge is 4.9 l/s, there is no sediment supply upstream, the upstream slope is 0.004 and the downstream slope is 0.02. These latter values respectively correspond to a mild and to a steep slope.

7.2.2. Numerical modelling

7.2.2.1. Two-velocity two-concentration model

Calibration of the two-layer friction coefficients

The friction coefficients are calibrated on the basis of uniform flow conditions, as exposed in chapter 6. For a given slope (or Froude number) and a given water discharge, the uniform depth is calculated with the Manning formula while the solid discharge and the critical shear stress are evaluated with the Meyer-Peter–Müller formula as only bed-load is observed. The calibration conditions depend on the flow characteristics. In the present application, the flow is partly subcritical and partly supercritical. Then it was chosen to calibrate the friction coefficients using the parameters (q_w, h_w, q_s, S_0 and τ_{crit}) of a flow corresponding to $\mathrm{Fr}_w = 1$, which is a good average of the observed Froude number. The obtained calibrated values, corresponding to run 1 (Table 7.1), with a concentration in the transport layer $C_s = 0.22$, are $C_{f,w} = 0.025$, $C_{f,s} = 0.079$. In this case, the constant velocity ratio in uniform flow is $\alpha = 0.329$. If the calibrated friction coefficients are acceptable, the computed solid discharge should be close to Meyer-Peter–Müller predictions (Fig. 7.2) and the Manning coefficient should be close to the one deduced from measurements (Fig. 7.3).

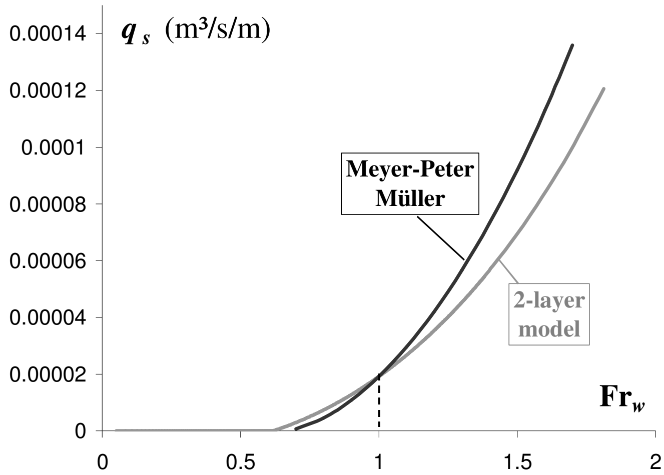

Figure 7.2. Evolution of solid discharge q_s with Froude number Fr_w : comparison between two-layer model and Meyer-Peter–Müller formula (run 1 (Table 7.1), $C_{f,w} = 0.02$, $C_{f,s} = 0.128$)

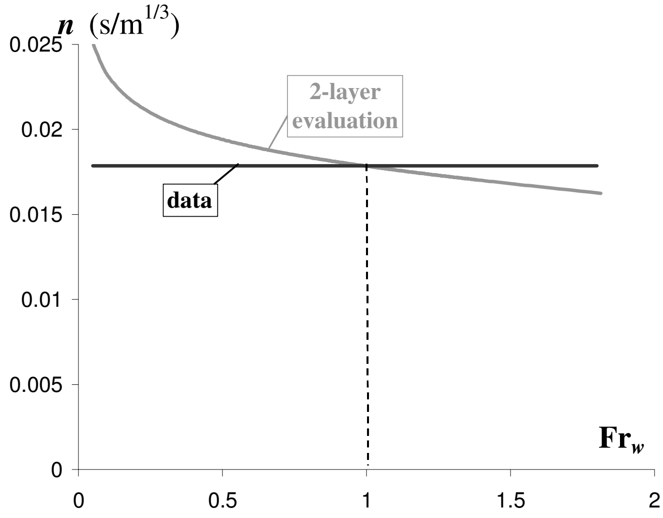

Figure 7.3. Evolution of roughness Manning coefficient n with Froude number Fr_w : comparison between two-layer model and data (run 1 (Table 1), $C_{f,w} = 0.02$, $C_{f,s} = 0.128$)

The solid discharge q_s is overestimated for subcritical Froude numbers and underestimated for supercritical Froude numbers. In the range of $Fr_w = 0.8 \ldots 1.3$, corresponding to the solid transport most often observed during the experiment, the estimations of the two-layer model and the Meyer-Peter–Müller formula are close. The Manning coefficient (labelled as data) is an estimation of the average experimental Manning coefficient. The difference between this constant coefficient and the one deduced from the two-layer model is mainly due to the difference between Manning formulation, used for calibration, and Chézy form, used to express the shear stresses (chapter 6).

Boundary conditions

The non-dimensional number Z_{sw}, which is important in the boundary conditions treatment, is calculated for a range of water Froude numbers, with the friction coefficients calibrated above and in the case of uniform flow conditions (Fig. 7.4).

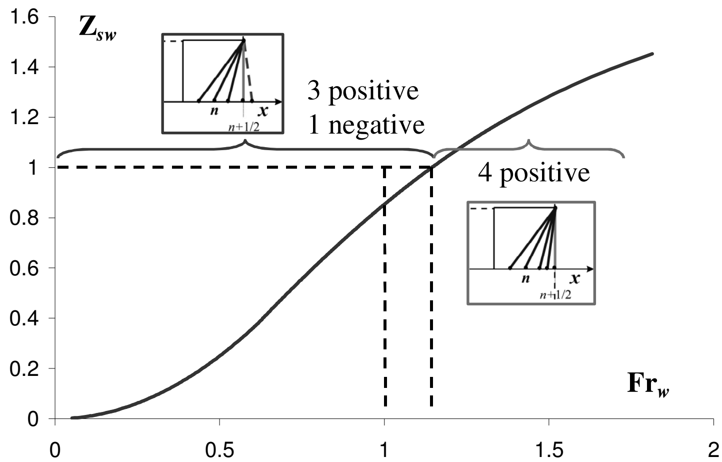

Figure 7.4. Evolution of the number Z_{sw} computed with the water Froude number Fr_w , ($C_{f,w} = 0.02$, $C_{f,s} = 0.128$)

Two zones can be distinguished on the basis of the boundary conditions treatment summarised in Table 4.6 of chapter 4:

- Fr_w<1.15: (Z_{sw}<1) three positive and one negative eigenvalues implying three upstream (e.g.: q_w, q_s, h_s) and one downstream (e.g.: h_w or control section) boundary conditions
- Fr_w>1.15: (Z_{sw}>1) four positive eigenvalues implying four upstream boundary conditions (e.g.: q_w, q_s, h_w, h_s)

The flow at the upstream boundary remains subcritical during the experiment and three upstream boundary conditions have to be imposed. The flow at the downstream boundary remains always supercritical during the experiment and the number of downstream boundary conditions will depend on the non-dimensional number Z_{sw}. Till the Froude number is higher than 1.15, there is a total transmission without any downstream boundary condition. If the Froude number decreases below 1.15, the downstream end may influence the flow and a boundary condition has to be imposed (Fig. 7.5).

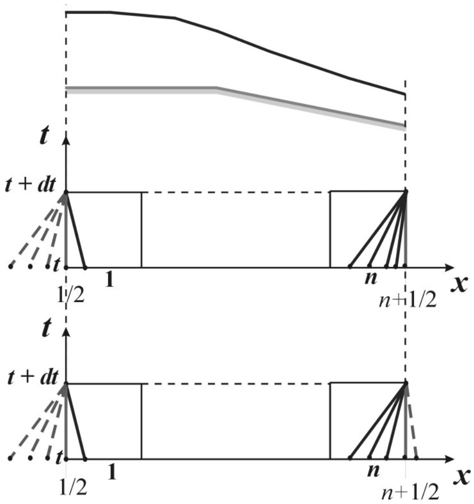

Figure 7.5. Two-layer boundary conditions in the case of the knickpoint migration transcritical case

The eigenvalues are ranked from the highest to the lowest. The unknowns at the upstream interface ($h_{w,1/2}$, $h_{s,1/2}$, $z_{b,1/2}$, $q_{w,1/2}$, $q_{s,1/2}$) are obtained by the resolution of a system composed of the following three boundary conditions

$$q_{w,1/2} = q_{w,up} = 0.0098 \text{ m}^3\text{/s/m} \qquad q_{s,1/2} = q_{s,up} = 0 \qquad h_{s,1/2} = 0 \quad (7.1)$$

closed with two compatibility relations. One is linked to the vertical characteristic (eigenvalue $\lambda_4 = 0$) and another is linked to the negative characteristic (negative eigenvalue λ_5) (chapter 4).

In the case of 4 positive eigenvalues downstream ($Z_{sw} > 1$), the unknowns at the downstream interface ($h_{w,n+1/2}$, $h_{s,n+1/2}$, $z_{b,n+1/2}$, $q_{w,n+1/2}$, $q_{s,n+1/2}$) are obtained by the resolution of a system composed of the five compatibility relations, which can be simplified to express a total transmission.

$$h_{w,n+1/2}=h_{w,n} \qquad h_{s,n+1/2}=h_{s,n} \qquad q_{w,n+1/2}=q_{w,n}$$

$$q_{s,n+1/2}=q_{s,n} \qquad z_{b,n+1/2}^{t+dt}=z_{b,n+1/2}^{t} \tag{7.2}$$

If one of the eigenvalue is negative downstream ($Z_{sw} < 1$), even if the flow is supercritical, a boundary condition has to be imposed at the downstream end. This case will be exposed below.

The bed level at the downstream end constitutes a point around which the bed pivots. At this point, the bed elevation is imposed as constant throughout the time, i.e. like an non-erodible bed level.

$$z_{b,n+1/2}^{t+dt} = z_{b,n+1/2}^{t} = z_{b,\text{fixed}} \tag{7.3}$$

Comparisons

For numerical modelling, the domain of calculation is discretised in 1 cm-long cells, and the time step is calculated in order to respect the CFL condition with a CFL number of 0.7. The second order accuracy in time and space of the algorithm is applied. The experimental and computed initial conditions are plotted on Figure 7.6. All Figures are plotted with the same conventions : time $t = 0$ corresponds to the initial condition and the origin of the horizontal co-ordinates (in meters) is placed at the upstream end of the flume. The computed initial bed level is compound of two constant slopes, contrarily to the experimental one, which is more irregular. The non-erodible bed, corresponding to the bottom of the flume, is set to 0.11 m.

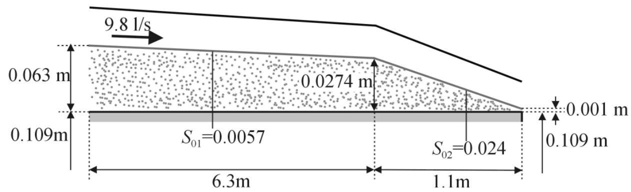

a)

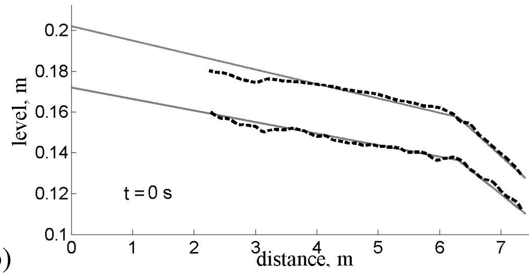

b)

Figure 7.6. (a) Initial conditions (b) Comparison between experimental (▪▪▪▪) and computed (▬) levels : initial conditions

Figure 7.7 illustrates the time-evolution of the water and the bed levels. Due to the regressive erosion, the slope upstream of the knickpoint increases while the slope downstream of it decreases. The erosion continues until the two slopes become similar leading the knickpoint and the control section to vanish. The bed level at the downstream end remains constant during the whole computation and the downstream slope decreases, taking this fixed point as rotation point. There is no sediment supply upstream; thus, the flow erodes a part of the bed at the upstream end to constitute a transport layer. This erosion area enlarges downstream with time. In the downstream part, the computed bed level is a little higher than the experimental one. As presented in the calibration section (Fig. 7.2), for high Froude numbers, the computed solid discharge is a little lower than the one estimated by Meyer-Peter–Müller, a lower erosion in this area is induced. Moreover, when the Froude number is lower than 1 (upstream of the knickpoint), the solid discharge is overestimated in comparison with Meyer-Peter–Müller predictions. An overestimated solid discharge in the upstream reach induces an overestimated erosion resulting in a bed level upstream, which is lower. For subcritical flow, the Manning coefficient is overestimated which leads to an overestimation of the computed water depth. As the bed and water levels are not measured in the upstream part of the flume, no comparison near the upstream boundary is possible.

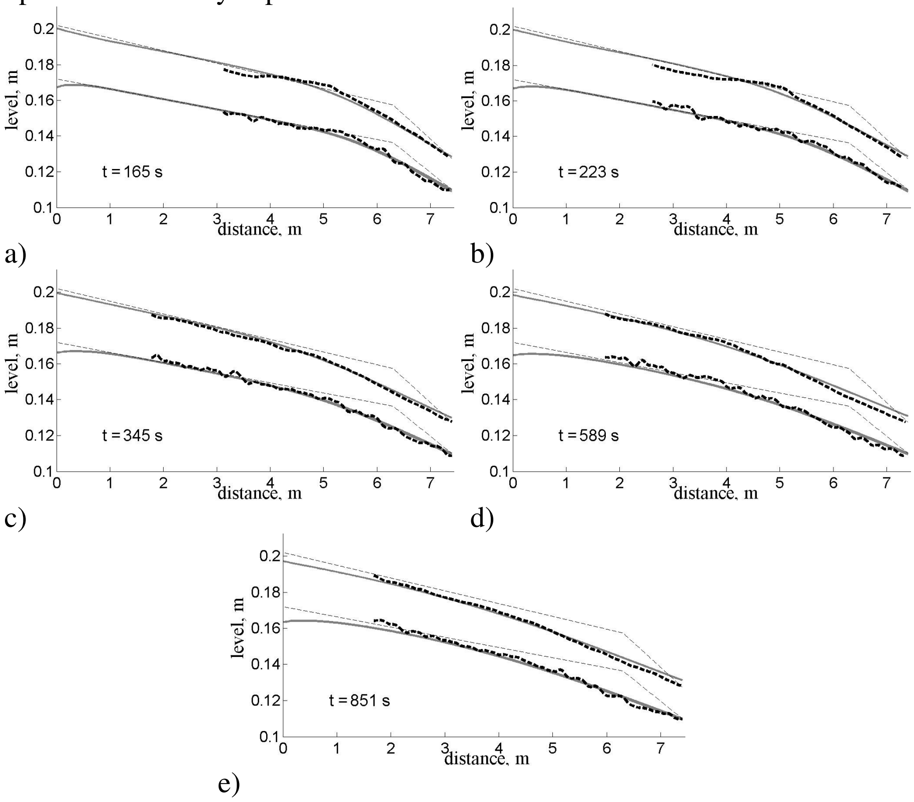

Figure 7.7. Comparison between experimental (▪▪▪▪) and computed (——)levels : time-evolution (108 s – 851 s) (initial conditions (- - -))

The evolution of the solid discharge along the flume with time is plotted in Figure 7.8. In initial conditions, there is no transport layer, thus the solid discharge is equal to zero everywhere. The time-evolution delimits three zones.

- The upstream part of the flow (distance < ~1.8 m) corresponds to the creation of the transport layer. The reach without any solid discharge elongates with time. The slope and the solid discharge decrease with time in this reach. At the upstream end, the solid discharge is zero (imposed boundary condition), but, in the first computational cell, it already takes a non-zero value. The shear stress applied to the bed never decreases below the threshold value, as a solid transport is always calculated.

- The middle zone (1.8 m < ~ distance < ~ 6 m) is the part of the flow located between the knickpoint and the upstream reach. At the beginning of the experiment, a water profile M_2 develops from the critical depth at the knickpoint. As the length is important enough and the slope is quite regular, the water profile reaches the uniform depth upstream. For the first computational steps, there is a zone (~=2 m or 2.5 m) where the flow is close to be uniform and the solid discharge is close to equilibrium. The solid discharge increases approaching the knickpoint and with time, inducing a steepening of slope.
- The zone downstream of the knickpoint, is the part where the flow is supercritical. At the beginning of the experiment, the solid discharge increases sharply in this area. Due to the regressive erosion, the solid discharge and the bed slope decrease with time in this part of the flow.

At the end of the experiment/computation, the knickpoint vanishes and the different areas become less distinguishable.

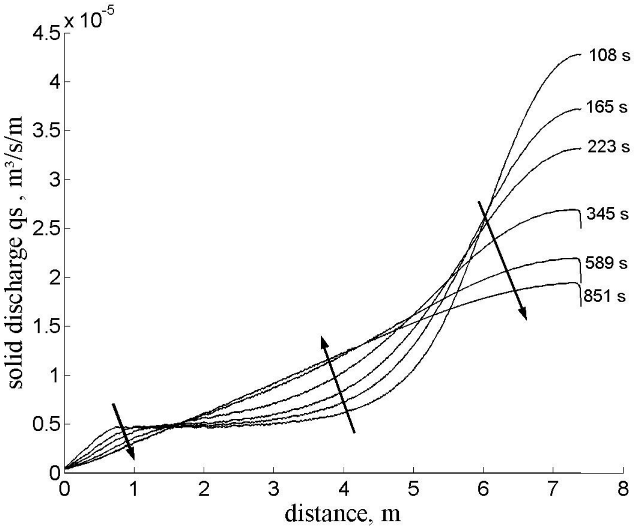

Figure 7.8. Time-evolution of the computed solid discharge q_s along the flume

Even if the transport layer depth h_s is set to zero at the upstream interface, the flow generates a transport layer in the first cell (Fig. 7.9).

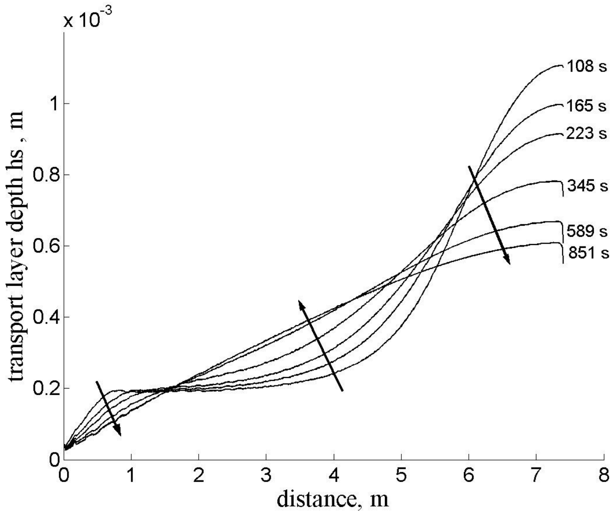

Figure 7.9. Time-evolution of the computed transport layer depth h_s along the flume

Except at the entrance of the flume, the velocity ratio $\alpha = u_s/u_w$ is quite constant ($u_s\,/\,u_w \approx 0.31$) along the flume (Fig 7.10). There is little variation of this ratio with time and it is slightly different from the predicted value in uniform flow conditions. This difference is due to the fact that the uniform flow conditions are not present.

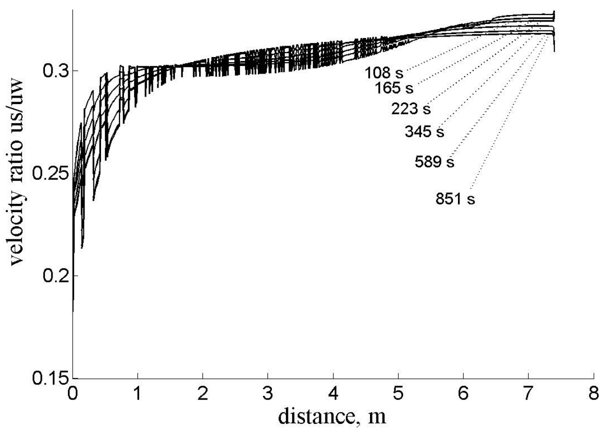

Figure 7.10. Time-evolution of the computed ratio $u_s\,/\,u_w$ along the flume

Equilibrium state is not reached during the experiment. Since no sediment is supplied upstream, the prolongation of the experiment would not lead to an equilibrium state with solid transport either. The equilibrium would be reached when the shear stress applied to the bed would decrease under the resistant shear stress. As a result, deposition would occur and then, no transport would be observed anymore.

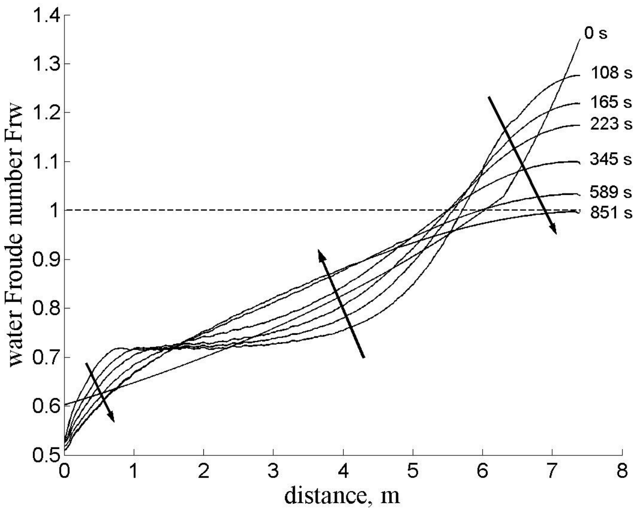

Figure 7.11. Time-evolution of the computed water Froude number Fr_w along the flume

The water Froude number (Fig. 7.11) and the solid discharge (Fig. 7.8) are closely linked, the three parts described above appear in both Figures. In the upstream reach, the flow becomes more and more subcritical with time, meaning the slope and the Froude number decrease. In the middle reach, the slope and the Froude number increase with time. Downstream of the knickpoint, the regressive erosion makes the slope and the Froude number decrease. During all the experiment, the flow remains transcritical. The movement of the control section is depicted in Figure 7.12. The control section propagates first upstream and then downstream in a space interval smaller than 1 m (during the experiment). When the non-dimensional number Z_{sw} becomes lower than 1 ($t > 345$ s) (Fig. 7.13), the downstream end influences the flow and the knickpoint stops propagating upstream to move downstream. The intuition, mentioned before, and exposed previously by other authors (for example: Brush and Wolman, 1960), that the knickpoint propagates upstream is thus only partly confirmed by the numerical results. Unfortunately the profiles are not smooth enough to observe the movement of the control section experimentally. At the end of the computational time, the knickpoint reaches the downstream end and the flow becomes subcritical all along the flume.

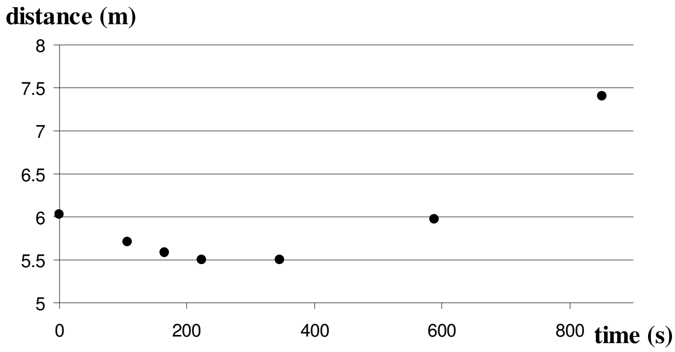

Figure 7.12. Position of the control section along the flume with time

For the last three computational times (345 s, 589 s and 851 s), the non-dimensional number Z_{sw} (Fig. 7.13) is lower than 1 at the downstream end ($Fr_w < 1.15$). As a result, one boundary condition has to be imposed at the downstream end. However, looking at the experiment, the choice for this condition is not obvious. A parallelism is made with a pure hydrodynamic example (Fig. 7.14) where a supercritical water profile S_2 develops on a steep-sloped flume. If the slope decreases under the critical slope, the flow becomes subcritical and the water profile becomes M_2. The location of the control section changes from the upstream to the downstream end. If the slope decreases again, the downstream condition remains a critical section $Fr_w = 1$ (corresponding to an eigenvalue equal to zero). In the case of a two-layer flow, when the slope decreases, the non-dimensional number Z_{sw} decreases till it reaches 1 at the downstream end. Then, the influence on the flow moves from the upstream to the downstream end. If the slope decreases again, there is a kind of mixed control section at the downstream end, where the non-dimensional number Z_{sw} remains equal to 1 (corresponding to an eigenvalue equal to zero).

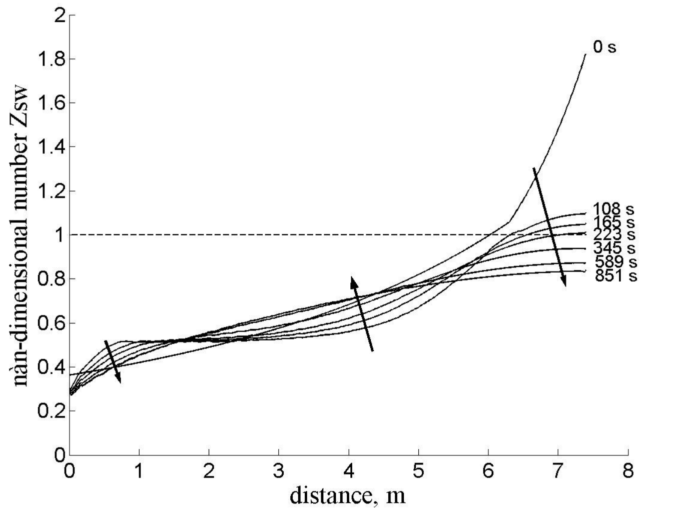

Figure 7.13. Variation of the computed non-dimensional number Z_{sw} along the flume with time

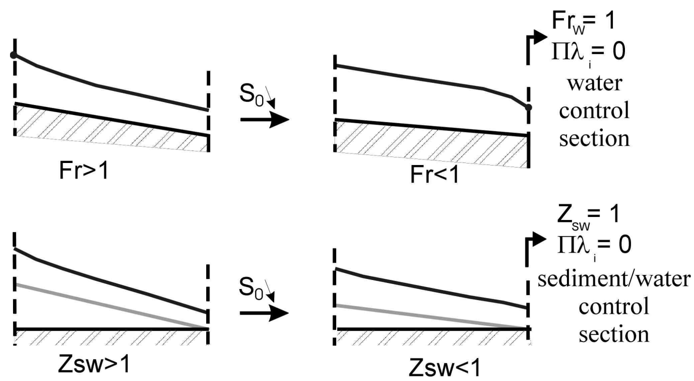

Figure 7.14. Comparison with the hydrodynamic case, control section

In this case, one of the compatibility relations has to be replaced by a mixed control section condition. Z_{sw} is fixed to 1, implying one of the eigenvalue is set to zero.

The real and imaginary parts of the five eigenvalues are plotted in Figure 7.15a-b at time 108 s and in Figure 7.16a-b at time 851 s.

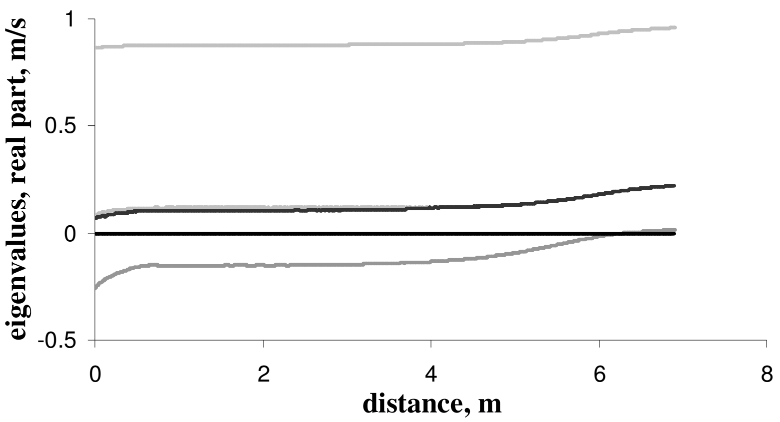

a)

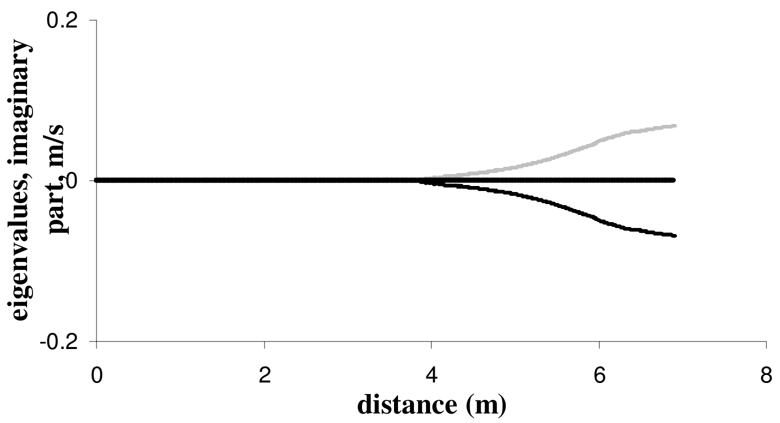

b)

Figure 7.15. Real (a) and imaginary (b) parts of the eigenvalues for t = 108 s

A part of the computational domain, which extends upstream with time, corresponds to a non-hyperbolic problem. When all the eigenvalues are real, the two internal eigenvalues are close and they become closer and closer, till they become conjugate complex. The real parts of the internal eigenvalues do not show any discontinuity between the hyperbolic and in the non-hyperbolic regions. A presumption is that the loss of hyperbolicity corresponds to the loss of a degree of freedom. In this case, in the non-hyperbolic region, a specific link between the variables would exist and the two characteristics, corresponding to the internal eigenvalues, would be reduced to one. In the algorithm, only the real part of the internal eigenvalues is considered, leading to two identical characteristics.

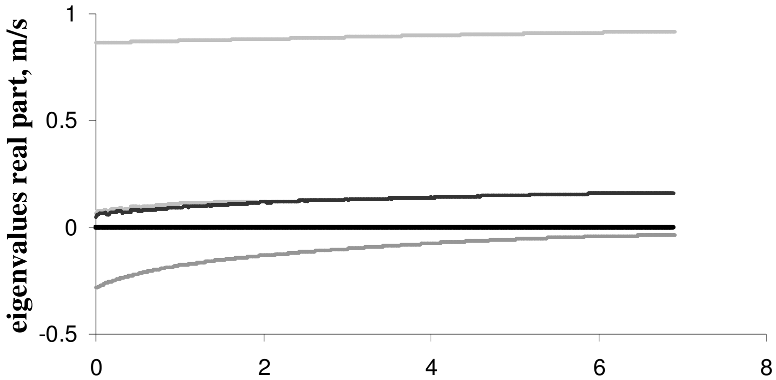

a)

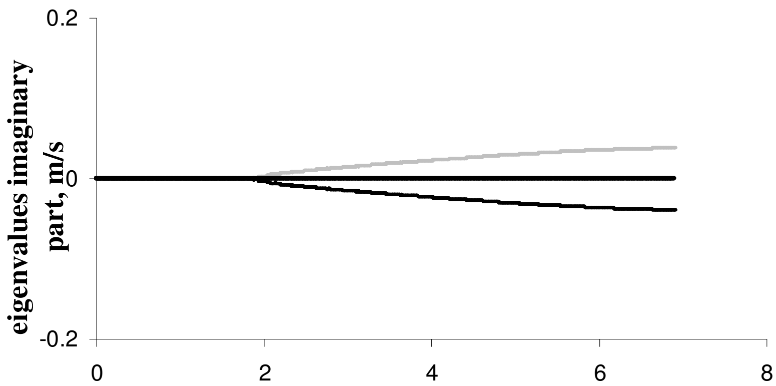

b)

Figure 7.16. Real (a) and imaginary (b) parts of the eigenvalues for t = 546 s

7.2.2.2. Influence of the assumption on the sediment concentration

In this section, the sediment concentration is assumed to be identical in the transport layer and in the bed $C_s = C_b = 0.57$ (Capart and Young, 2002). As exposed in chapter 6, the calibration values of the friction coefficients are influenced by the concentration in the transport layer. The obtained calibrated values, corresponding to run 1 (Table 7.1) are $C_{f,w} = 0.0258$, $C_{f,s} = 0.0495$, the sediment friction coefficient is more affected by the change in concentration. The constant velocity ratio under uniform flow conditions is not greatly affected, becoming $\alpha = 0.34$ instead of 0.329. The main impact of the change in concentration concerns the boundary conditions, which are influenced by the non-dimensional number Z_{sw} (Fig. 7.17). The reach where the flow is supercritical with one negative eigenvalues ($Z_{sw} < 1$) is reduced. The transport layer takes less space in the flow when the concentration is small, its influence on the global behaviour of the flow is then decreased.

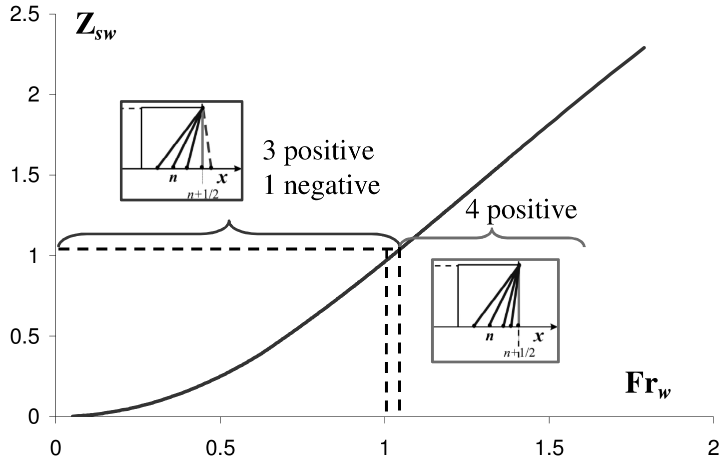

Figure 7.17. Variation of the non-dimensional number Z_{sw} with the Froude number Fr_w

For Froude numbers greater than 1.05 (previously, in Figure 7.4, it was 1.15), there is a total transmission at the downstream end. Else, one boundary condition has to be imposed downstream.

The bed and water profiles are compared to those previously calculated in the case of the two-concentration model for t = 108 s and t = 851 s (Fig. 7.18). For computational times between 100 s and 400 s, instabilities appear in the supercritical part (Fig. 7.18a-b), but the upstream subcritical part is not affected. These instabilities develop through several computational cells and progress upstream. They seems similar to antidunes in supercritical flow, but this similitude could only be apparent and no assertive conclusion may be deduced. In the experiment it is difficult to affirm their presence as the bed profiles present irregularity during the whole experiment.

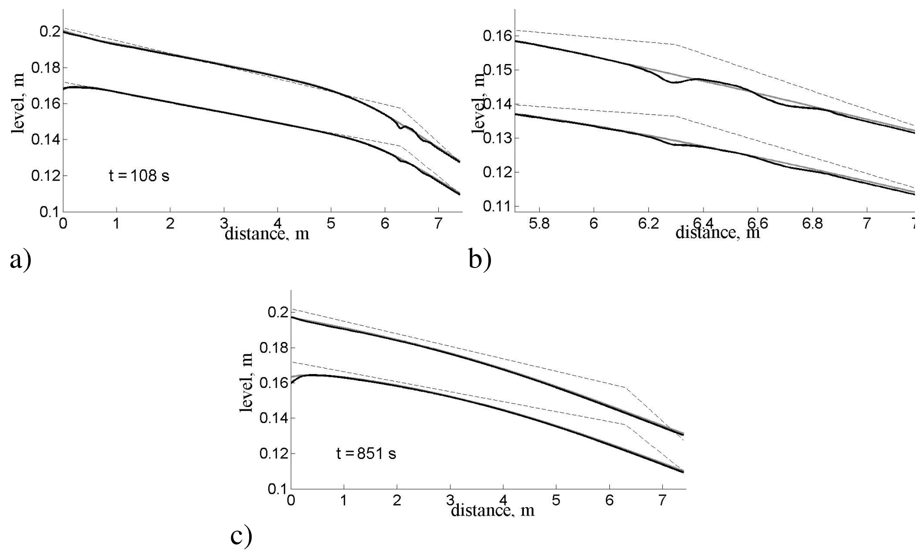

Figure 7.18. Comparison between computed levels with $C_s = C_b = 0.57$ (▬) and with $C_s = 0.22$ (▬): time evolution (a-b) for t = 108 s (c) for t = 851 s (initial conditions (- - -))

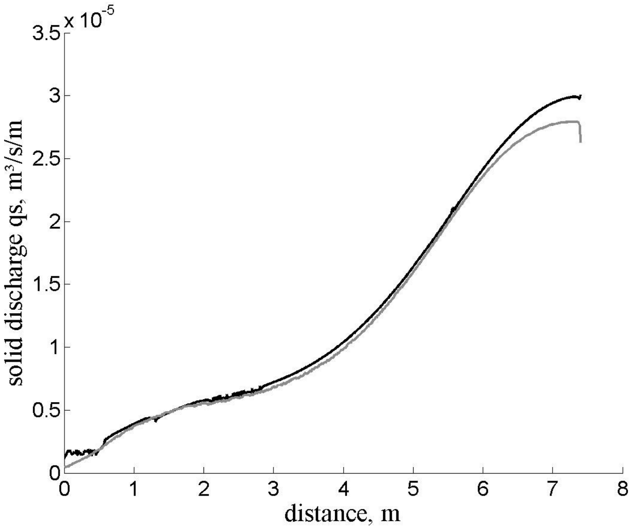

Figure 7.19. Comparison of the computed solid discharge q_s along the flume, when $C_s = C_b = 0.57$ (▬) with $C_s = 0.22$ (▬) for t = 851 s

When instabilities are over, or in the part of the flow, which is not perturbed, the two models give similar results (Fig. 7.18c). When the concentration is lower, the solid discharge is slightly more important, inducing a little more erosion at the upstream end (Fig. 7.19).

Similarly to the two-concentration model, the velocity ratio remains constant in space and does not change a lot in time. Contrarily to the previous case, the flow remains transcritical during the whole computation. While the control section propagates upstream, its evolution is not dependant on the concentration. On the contrary, downstream, the control section propagation is faster when the concentration is low (Fig. 7.20).

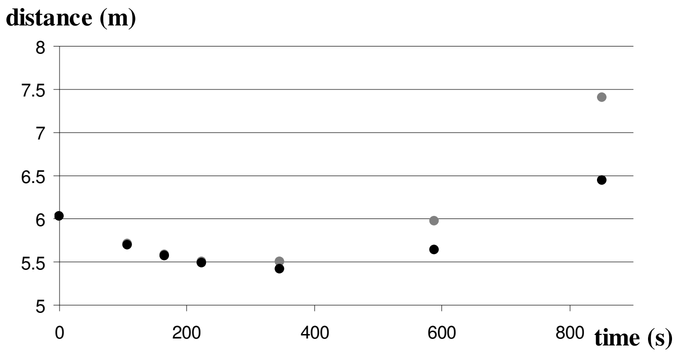

Figure 7.20. Position of the control section along the flume with time when $C_s = C_b = 0.57$ (•) with $C_s = 0.22$ (•)

As announced (Fig 7.17), the behaviour of the flow at the downstream boundary is not identical in both cases. In the one-concentration model, the non-dimensional number decreases below 1 only at the end of the computation (Fig. 7.21). It can be noticed that the instabilities are not generated by the boundary conditions, as there is a small region downstream where no perturbation occurs

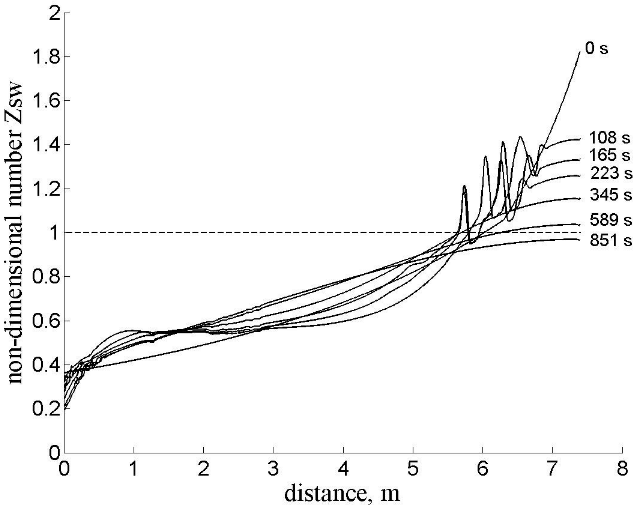

Figure 7.21. Variation of the computed non-dimensional number Z_{sw} along the flume with time ($C_s = C_b = 0.57$)

Contrarily to the two-concentration case, the zone where the problem is non-hyperbolic corresponds to a part of the domain where the non-dimensional number $Z_{sw} > 1$. The size of this zone reduces with time and, at the end of the computation, the whole domain is hyperbolic.

If the friction coefficients are calibrated on another transport formula, e.g. giving a 20% lower solid discharge ($C_{f,w} = 0.02$, $C_{f,s} = 0.11$), the instabilities disappear. The presence of instabilities is linked to the value of the friction coefficients and then to the sediment transport layer characteristics. With these parameters values, the results of the computation are still close to the experimental ones. The only variation is coming from the bed level, which is slightly higher (mainly at the upstream end).

7.2.2.3. Influence of the assumption on the velocity

The constant velocity ratio model provides an alternative solution, which remains always hyperbolic. In this case, the calibration values of the friction coefficients remain identical ($C_{f,w} = 0.025$, $C_{f,s} = 0.079$). The constant velocity ratio $\alpha = 0.329$ is deduced from the calibration. This value, corresponding to uniform flow conditions, is not too far from the one obtained when no relation is imposed between the velocities ($\alpha \approx 0.31$ in Figure Fig 7.10). The number of eigenvalues is reduced to four and two boundary conditions, instead of three, have to be imposed upstream, the boundary condition on h_s disappears. There is also one less compatibility relation downstream, the number of downstream boundary conditions now depends on the value of the mixed Froude number Fr_{sw}. The comparison between both non-dimensional numbers Z_{sw} and Fr_{sw}, in case of uniform flow, is plotted in Figure 7.22 for various Froude number Fr_w. When there is no solid transport, for low Froude numbers, both numbers are identical and equal to Fr_w^2. In other cases, the non-dimensional number Z_{sw} is lower than the mixed Froude number Fr_{sw}. As a result, the mixed control section of the two-layer flow occurs for lower water Froude number when the velocities are explicitly linked ($Fr_{sw} = 1$) if compared to the two-velocity model ($Z_{sw} = 1$). The zone where a downstream boundary condition is needed is wider for the two-velocity model.

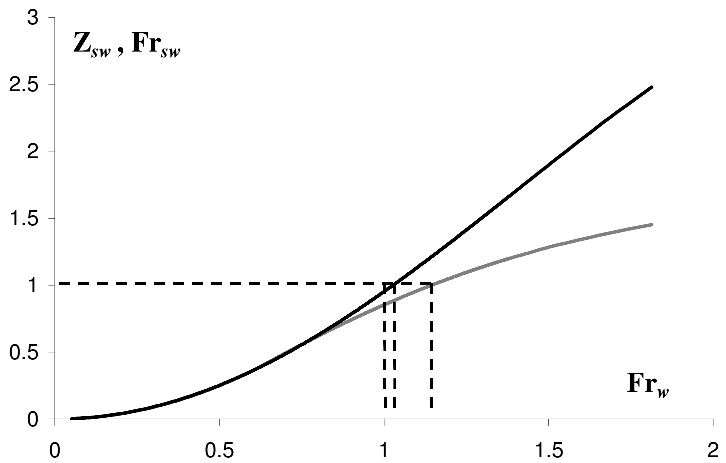

Figure 7.22. Variation of the non-dimensional numbers Z_{sw} (▬) and Fr_{sw} (▬) with the Froude number Fr_w

The bed and water profiles are identical to those obtained for the two-velocity model during the whole computation, except at the extreme upstream part of the flume, where more erosion take place with the two-velocity approach. As both models are very close, only profiles corresponding to the final computational time, where the most important difference is noticed, are presented (Fig. 7.23).

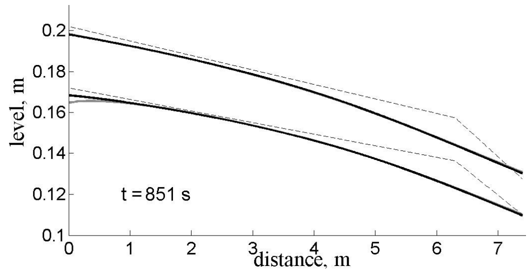

Figure 7.23. Comparison between computed levels with the two-velocity model (▬) and with the constant velocity ratio model (▬) for t = 851 s (initial conditions (- - -))

The difference between the two models at the upstream end of the flume is due to the difference in the solid discharge estimation (Fig. 7.24). As this difference is not very large, it mainly has an influence at the beginning of the channel, where the sediment transport layer has to be created. Then the additional discharge, calculated by the two-velocity model, is transmitted downstream. This transmission implies that no additional erosion downstream is necessary to feed the transport layer, even if the corresponding solid discharge is more important. It explains why the bed level deduced from both models is identical except upstream.

As the water and bed profiles are identical in both models, the propagation of the control section is also the same in the two models. Contrarily to the two-velocity model, a downstream boundary condition has to be imposed only during the last computational times, when $Fr_{sw} < 1$.

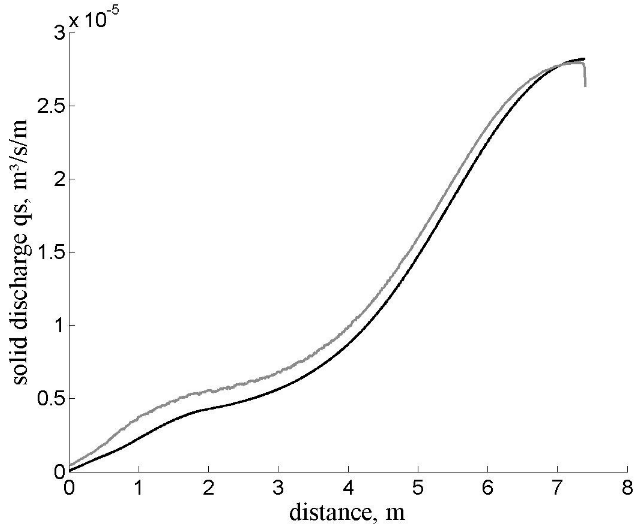

Figure 7.24. Comparison of the solid discharge q_s along the flume, computed with the two-velocity model (▬) and with the constant velocity ratio model (▬) for t = 851 s

The eigenvalues (which are always real) of the constant velocity ratio model (in red) are computed for t = 108 s and t = 851 s and compared (Fig. 7.25) to the real part of the ones obtained previously (Figs.7.15a and 7.16a) for the two-velocity model.

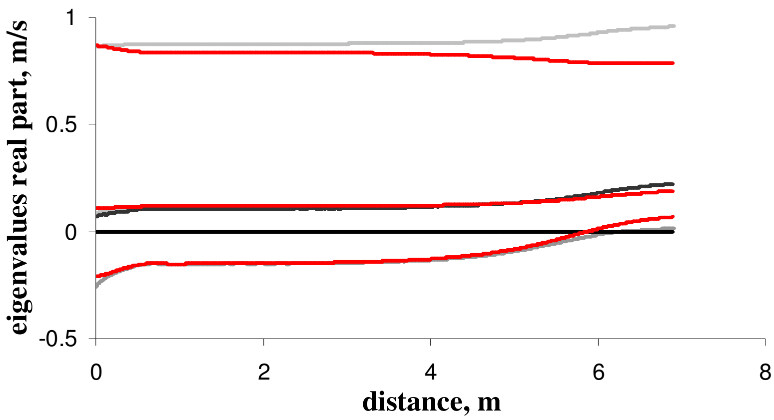

a)

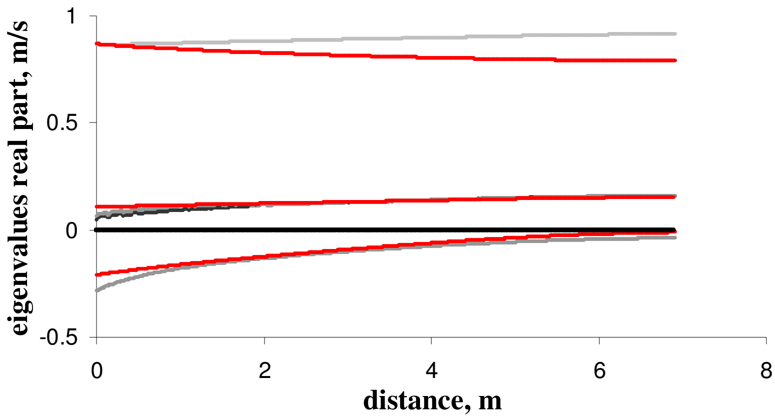

b)

Figure 7.25. Comparison between the eigenvalues of the constant velocity ratio model (—) and the real part of the eigenvalues of the two-velocity model (a) for t = 108 s (b) for t = 546 s

The difference at the upstream end is explained by the fact that the bed and the water levels in this part of the flume are not identical for both models. Even if they are in the same range of values, the external eigenvalues calculated for both models are quite different. On the other hand, the real part of the internal eigenvalues obtained for the two-velocity model is quite close to the real internal eigenvalue corresponding to a constant velocity ratio. The difference is slightly more important in the supercritical part of the flow. This similarity gives the feeling that the real part of the eigenvalues in the case of the two-velocity model should not be too far from the physical celerity of information. It would explain why, even if the eigenvalues are complex in the two-velocity model, taking the real part of the eigenvalues does not lead to important mistakes nor instabilities.

7.2.2.4. Comparison with Saint-Venant – Exner

The Saint-Venant – Exner numerical model used in this thesis was developed by Goutière and Laraichi (2006), in their diploma work. In this model, the bed level is deduced from the Exner equation (2.9), which becomes when discretised in finite-volume

$$z_{b,i}^{n+1} = z_{b,i}^{n} + \frac{dt}{dx}\left(q_{s,i-1/2}^{*} - q_{s,i+1/2}^{*}\right) \tag{7.4}$$

where $z_{b,i}^{n+1}$ is the bed level in the computational cell i at time $n + 1$, deduced from the bed level at the same place at time n and from the fluxes q_s* crossing the interfaces of the cell. The general HLL formulation of the fluxes (3.22) yields

$$q_s^{*} = \frac{S_R q_{s,L} - S_L q_{s,R} + S_L S_R \left(z_{b,R} - z_{b,L}\right)}{S_R - S_L} \tag{7.5}$$

The diffusive term $S_L S_R \left(z_R - z_L\right)/S_R - S_L$ induced by the level variation is appropriate only if a fluid is concerned. As the bed is concerned, due to its solid property, the diffusive term induced by the bed level variation has no physical meaning, making this expression inappropriate. Instead, the solid discharge is supposed to be the mean value of the solid discharge in the neighbouring cells

$$q_s^{*} = \frac{q_{s,L} + q_{s,R}}{2} \tag{7.6}$$

The flow is divided into two parts (Fig. 7.26): the reach located upstream of the knickpoint (subcritical) and the one located downstream of it (supercritical). In each reach two conditions have to be imposed upstream and one downstream of it. As summarised in Table 4.2 of chapter 4, it is usually stated that in supercritical flows, the two upstream conditions (linked to the positive eigenvalues) concern the hydrodynamic variable (h_w and q_w) and the downstream one (linked to the negative eigenvalues) concerns the sediments (z_b). By the same way, in subcritical flow, conditions on hydrodynamics have to be imposed upstream (q_w) and downstream (h_w), while the second upstream condition concerns the sediments (z_b). As the two parts are merged, the bed level z_b should be imposed upstream and downstream and the water discharge q_w should be imposed upstream.

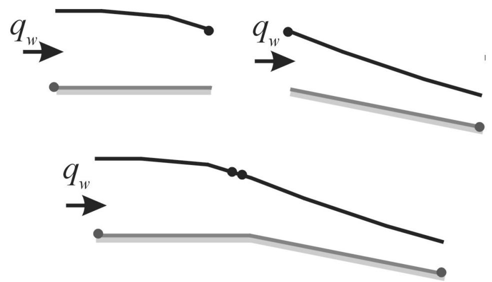

Figure 7.26. Classical boundary conditions in the case of the knickpoint migration transcritical case

However, in the experiment, as there is no sediment supply, the bed level at the upstream reach cannot be constant. The boundary condition on the bed level is not adapted to this case, imposing the solid discharge instead of the bed level would have been better. If, due to erosion, the flow becomes subcritical at the downstream end, a control section has to replace the boundary condition on the bed level. As it was the case for the two-layer model, the channel is divided in 1 cm-long computational cells and the CFL number is equal to 0.7. The computed bed and water levels are identical to those calculated with the two-layer model (less than 0.5 mm difference), except at the upstream extremity. The profiles obtained with both models are plotted for t = 851 s in Figure 7.27. The bed-level calculated with Saint-Venant – Exner has to be compared to the bed level z_b computed with the two-layer model. In fact, the depth h obtained with the Saint-Venant – Exner model is a total depth, which is supposed to be equivalent to the sum of the water and the sediment transport layers.

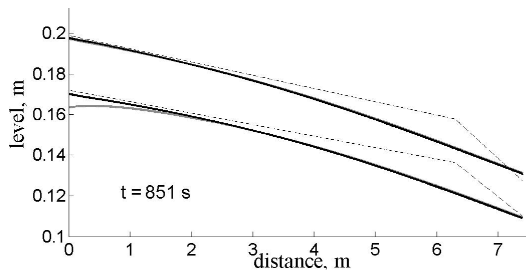

Figure 7.27. Comparison between computed levels with the two-velocity model (▬) and with the Saint-Venant – Exner model (▬) for t = 851 s (initial conditions (·····))

The difference of bed-level upstream is due to the difference between the solid discharges calculated by both models. Even if the two-layer model is calibrated on the Meyer-Peter–Müller formula, there is a distinction between both models (Fig. 7.28), due to the fact that the uniform flow conditions, used for calibration, are not present. The Meyer-Peter–Müller formula implemented in the Saint-Venant – Exner model assumes that the flow is in equilibrium everywhere, contrarily to the two-layer model. The variation of the solid discharge along the flume is similar, which explains why the bed levels are identical. The difference in solid discharge only induces a mismatch at the upstream end. The solid discharge at the upstream end is equal to zero at the beginning of the simulation. Small oscillations occur at the transition between the zones with and without solid discharge. A sediment transport takes place at the upstream end only at the end of the computation when the regressive erosion reaches this part of the flow. This erosion induces a decrease of the bed level in the first computational cell, even if the bed level is fixed at the upstream interface.

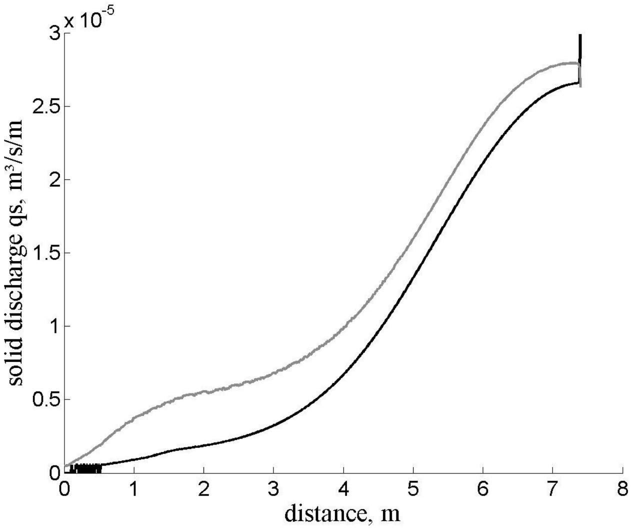

Figure 7.28. Comparison of the computed solid discharge q_s along the flume, with the two-layer model (—) and with the Saint-Venant – Exner model (—) for t = 851 s

As the profiles are identical, the Froude number follows the same evolution, meaning the control section migrates upstream at the beginning and downstream at the end of the simulation. At the end of the computation, all the flow is subcritical and a control section has to be imposed downstream. The three real eigenvalues of the Saint-Venant – Exner model (in red) are compared with the real part of those obtained with the two-layer model (Fig. 7.29).

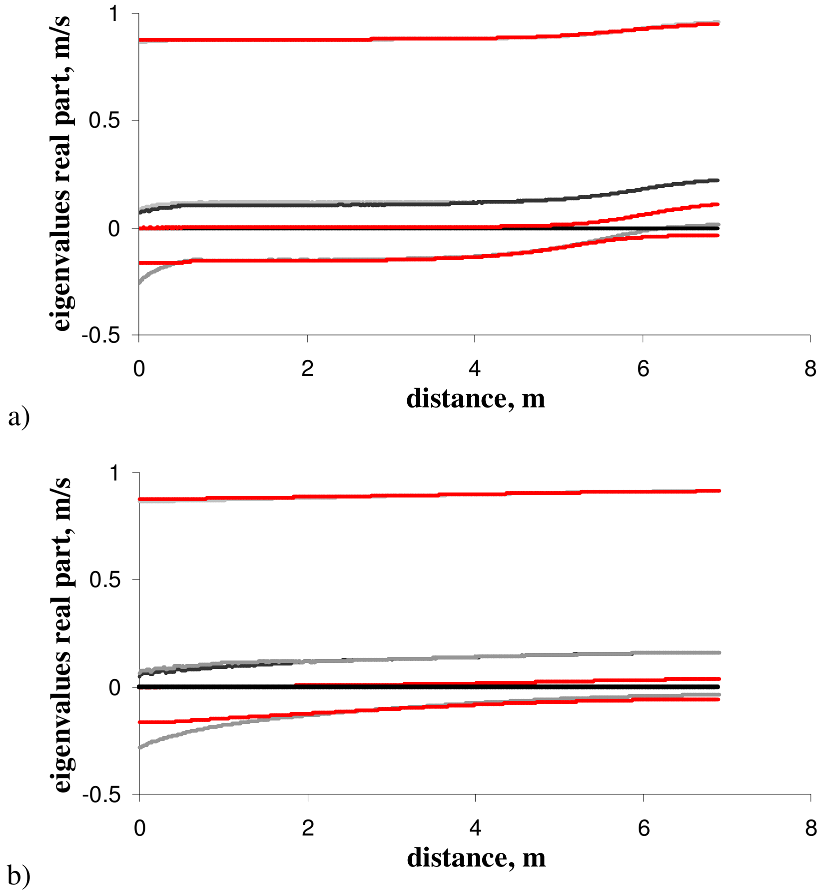

Figure 7.29. Comparison between the eigenvalues of the Saint-Venant – Exner model (—) and the real part of the eigenvalues of the two-layer model (a) for t = 108 s (b) for t = 546 s

The extreme eigenvalues are quite similar, except in the supercritical part of the flow for the smallest. The intermediate ones are different but their evolution in space (their slope) is comparable.

7.3. Hydraulic jump over mobile bed

7.3.1. Physical description

Mourad Bellal (Bellal et al., 2003) carried out a series of experiment to study the morphodynamic response of the river bed to the presence of a hydraulic jump (Fig. 7.30). The initial condition consists in a uniform supercritical flow fully developed throughout the channel length. The steep-sloped bed profile is in quasi-equilibrium and a constant sediment supply is supplied upstream (Fig. 7.30a). At reference time $t = 0$, this equilibrium situation is perturbed by the rapid raise of a submerged weir at the downstream end of the flume, imposing a subcritical condition. The so-generated hydraulic jump propagates upstream, altering the sediment transport capacity. In the supercritical part of the flow, the sediments remain in motion, but not in the subcritical part, implying the sediments depose at the transition, under the surge. As the jump moves upstream, the deposition area moves upstream too (Fig. 7.30b).

When the downstream water level is stabilised, the surge stops its propagation. As the surge now remains steady, the sediments accumulate at this location creating a sediment front. The continuous sediment supply from upstream progressively intensifies the front amplitude forcing it to migrate downstream. In turn, the hydraulic jump slowly propagates downstream, decreases in amplitude and progressively vanishes: the water discontinuity from super- to subcritical flow seems to be replaced by the sediment front (Fig. 7.30c).

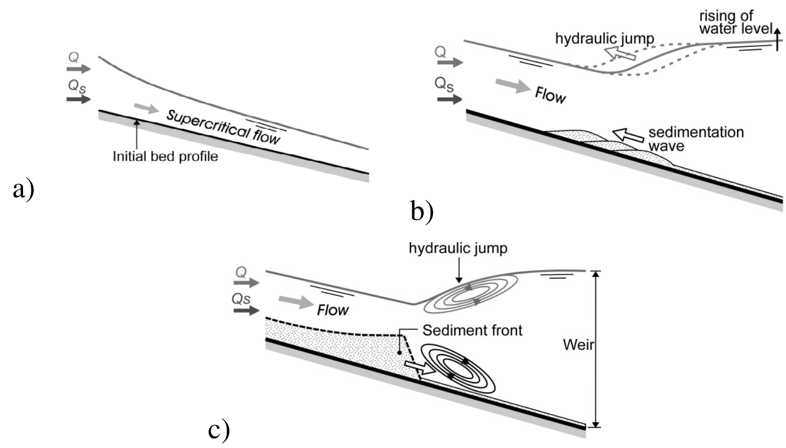

Figure 7.30. (a) Initial condition (b) Sedimentation wave (c) Sediment front propagation (Bellal et al, 2003)

In rivers, the sudden rise of the water level at the origin of the hydraulic jump can result, for example, from a sudden obstruction or from the presence of a check dam (Armanini et al., 2001; Busnelli et al., 2001) or a weir. Sieben (1999) proposed theoretical analysis of similar transcritical flow over mobile bed, detailing the different kinds of shock that may develop. More recently, Capart et al. (2006) proposed an approximated analytical solution based on the diffusion process to model the evolution of a semi-infinite sediment front.

Several experiments were performed within the following ranges of parameters (Table 7.2): initial bed slopes from $S_0 = 2$ % to $S_0 = 4$ %; liquid discharges from $Q_w = 11.5$ l/s to $Q_w = 15$ l/s; solid discharge $Q_s = 0.136$ l/s; the height of the submerged weir raised at time $t = 0$ is H_{weir}= 15.75 cm, the induced water level at the downstream end is $H_{w,\mathrm{down}}$ (column 8). Fr_0 (column 4) is the Froude number corresponding to initial uniform flow conditions; in column 5, Fr_w is the mean Froude number in the subcritical part of the flow (downstream of the sediment front) and in column 6, Fr_w is the averaged Froude number in the supercritical part of the flow (upstream of the sediment front). For all these test cases, the sand feeder is located at a distance of 0.7 m from the upstream end.

Run # (1)	S_0 (%) (2)	Q_w (l/s) (3)	Fr_0 initial (4)	Fr_w sub. (5)	Fr_w super. (6)	Q_s (l/s) (7)	$H_{w,\mathrm{down}}$ (cm) (8)
Run 1	3.55	11.5	1.92	0.13	1.14	0.136	20.86
Run 2	3.02	12	1.88	0.12	1.39	0.136	20.93
Run 3	2.74	15	2.47	0.13	1.27	0.136	22.63

Table 7.2. Experimental data (averaged values) (Bellal et al., 2003)

Two measuring systems were used: the bed profiler, successively measuring the bed and the water level, and the digital imaging (2 frame/sec). The advantage of the imaging process is its ability to track rapid changes in the bed and water profiles. It is very useful to measure the evolution of the sediment wave and the formation of the front, which occurs quickly in the second phase of the experiment. A sample image showing the development of the front is illustrated in Fig.7.31 (the image was rotated to be horizontal; one graduation corresponds to 1 cm).

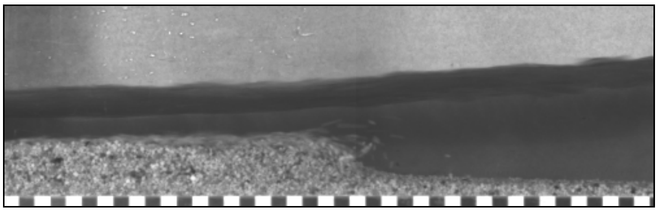

Fig. 7.31. Sediment front (Bellal et al., 2003)

The drawback of digital imaging is the video camera cannot be moved during the experiment and allows to capture images only in a limited window. The size of the window is limited to 0.9 m in order to maintain a sufficient accuracy (≈ 1 mm). The advantage of the bed profiler is the possibility to displace it and take measurements all along the flume. The disadvantage of the probe is the inability to have instantaneous measurements of the bed and water levels everywhere in the flume. The trolley, which supports the probe is trailed along the flume in one direction to measure the bed level and then in the opposite direction to measure the corresponding water level. It takes a little time, and is not appropriate when the changes are too rapid. The two measuring systems are complementary, digital imaging is used in the first stage of the experiment and the bed profiler is used in the second one.

7.3.2. Numerical modelling

7.3.2.1. Two-velocity one-concentration model

The above case is challenging for numerical modelling: a sudden change in the downstream boundary conditions ($t = 0$) forces a flow discontinuity in the channel, which is only possible to manage if boundary conditions are well posed and if the internal solver is shock-capturing.

Comparison is made with run 2 of the experiments (Table 7.2). The flow is modelled on a limited distance of 6.9 m. The upstream end of the numerical domain corresponds to the position of the sediment feeder, where the solid discharge is introduce in the flow ($x = 0.70$ m, as the origin is at the upstream end of the flume). The downstream end of the numerical domain corresponds to the weir at the end of the flume.

The sediment discharge entering the numerical domain is slightly different from the one supplied by the feeder. Due to the shape of the deposition under the feeder, some grains are not entering the modelled area (Fig 7.32). An estimation of the amount of grains deposing upstream is deduced from the repose angle of the sand. As a result, the estimated reduction of the discharge entering the flume is around 3 %. The solid discharge at the entrance of the modelled domain is then 0.000132 m³/s = 0.000264 m³/s/m. For more precision, the bed level should have been measured in the upstream reach of the channel, under the sediment feeder.

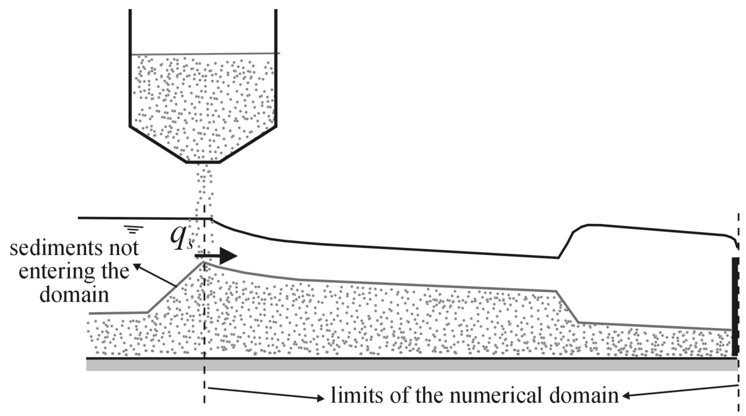

Fig. 7.32. Shape of the deposition under the sediment feeder

The initial slope corresponds to a steep slope. Downstream, a weir of 15.75 cm height is raised to make the water level increase. At the upstream reach, the flow is supercritical during the whole experiment and the four non-zero eigenvalues are positive. The upstream boundary conditions are the following: the liquid discharge $q_w = 0.024$ m³/s/m, the solid discharge $q_s = 0.000264$ m³/s/m, the water depth $h_w = 0.031$ m (less than the critical depth) and the thickness of the transport layer h_s, which is assumed to be at the equilibrium value corresponding to the solid discharge.

The downstream boundary conditions are the following: as far as the water level is under the level of the downstream weir, the flow is reflected ($q_w = 0$), while, once the weir is submerged, there is a liquid discharge at the outlet and a control section at the downstream interface. In this second stage, the subcritical flow passing over the weir is free of sediment. Then, the two intermediate eigenvalues, related to sediments, vanish and only the two external eigenvalues, corresponding to the pure hydrodynamic case, subsist. Among the remaining eigenvalues, as the flow upstream of the weir is subcritical, one is positive, and the other is negative. The negative characteristic is replaced by a boundary condition, which is, in this case, a control section.

The friction coefficients ($C_{f,w} = 0.015$, $C_{f,s} = 0.11$) are calibrated under steady uniform flow conditions (chapter 6). The coefficients are calibrated in order to match the uniform depth predicted by the Manning formula, and the sediment discharge deduced from the measurements. The sediment concentration in the transport layer is assumed to be identical to the concentration in the bed $C_s = C_b = 0.57$. The initial slope corresponds to a steep slope ($S_0 = 0.03$: for the computation, the initial bed level is assumed as the regression straight line through the experimental bottom level measurements). The experimental and numerical initial conditions are plotted on Figure 7.33. As initial condition, a sediment transport layer corresponding to the upstream solid discharge is imposed.

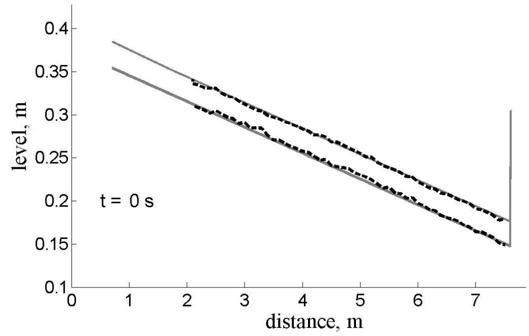

Figure 7.33. Initial conditions: numerical, experiment

In the first stage of the experiment (Fig. 7.30b), the surge propagates upstream, creating a deposition of sediment. Some numerical results are plotted in Figure 7.34. The sediments clearly depose under the surge, where the thickness of the transport layer reduces to zero (see Fig. 7.34f, which is a zoom of Fig. 7.34e, at time $t = 40$ s). Unfortunately this first stage is rather short and few measurements are available. Those few measurements (not represented here) reproduce the existence of the deposition area under the surge.

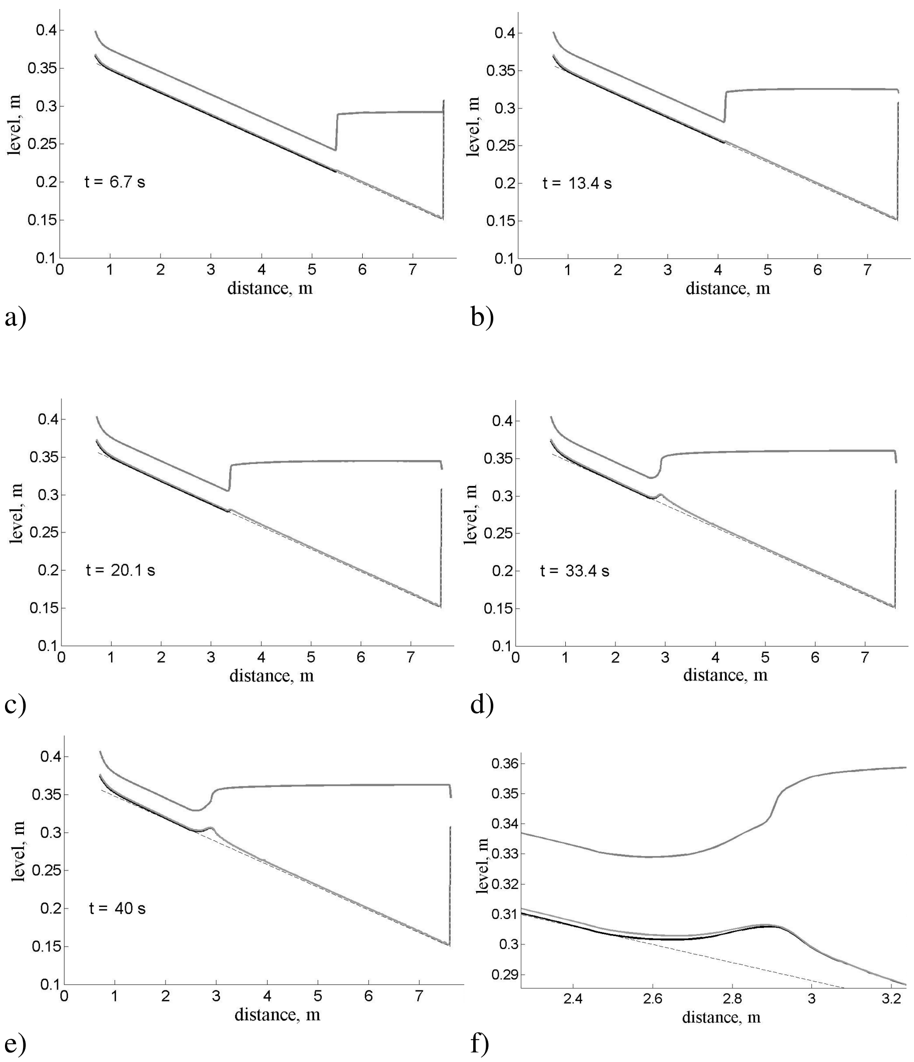

Figure 7.34. First-stage sedimentation wave propagation (numerical results)

z_w, z_s, z_b

When the surge reaches a steady location, all the sediments depose at the same place and the little sediment deposition area becomes a front. The experimental data concerning the front creation are compared to numerical results (Fig. 7.35) showing a good agreement. The experimental results are issued from digital imaging, explaining why they are limited to a window of 0.9 m.

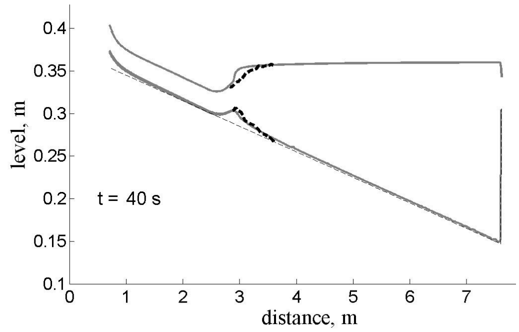

Figure 7.35. Front creation (numerical and experimental results), t = 40 s: - - - initial bed, ▬ numerical, ▪▪▪▪ experiment

In the second stage of the experiment (Fig. 7.30c), the sediment front propagates downstream with the hydraulic jump, numerical and experimental results are compared in Figure 7.36.

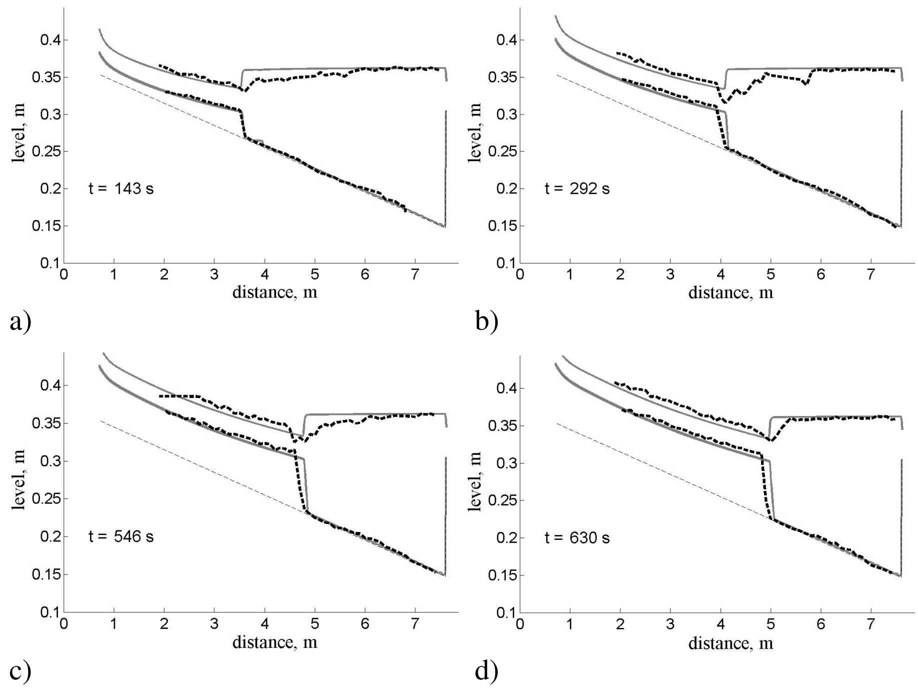

Figure 7.36. Second stage sediment front propagation (numerical and experimental results) - - - initial bed, ▬ numerical, ▪▪▪▪ experiment

This stage seems very similar to the delta formation in a reservoir but the presence of the hydraulic jump makes a significant difference. The measurements reproduced are those taken with the bed profiler.

The sediment front is well represented, nearly perfectly at the early stage, but there is a trend, for higher computational times, to slightly underestimate its amplitude and overestimate its celerity. The numerical sediment front is sharper than the experimental one. The model is not designed to take into account the physical bed instability corresponding to a too steep slope.

The water level is also well represented, except the fact that the jump representation is sharper than in the reality, which is not surprising for a shallow-water model, unable to take into account the complex velocity distribution of a jump.

The conservation of the sediment mass is satisfactory. Considering the numerical results (Fig. 7.37a), the evolution with time of the volume supplied by the feeder perfectly fits the integration of the computed bed profiles (the two curves are indistinct). Such a comparison is not completely possible for the experimental data, as the experimental profiles are not available at the upstream part of the flume. Nevertheless, the numerical and experimental evolutions of the sediment volume with time in the window between 2.1 m and 6.7 m, deduced from the integration of the respective bed profiles between these limits, are satisfactorily compared in Figure 7.37b.

Figure 7.38 shows the computed thickness of the transport layer h_s for various times. In the experiment, this thickness is reduced to zero at the toe of the sediment front, while in the numerical simulation a small thickness subsists (distance less than 4 m) at the beginning of the simulation. This is due to the fact that, in the model, at the toe of the front, the computed shear stress acting on the bed is greater than the theoretical critical shear stress, at least before the front reaches the distance of 4 m. To avoid numerical instabilities or non-realistic front celerities, a numerical trick is used consisting in equalling the solid discharge to zero if the transport thickness is lower than a fixed threshold value (10^{-8} m). This threshold value has to be small enough in order to maintain sediment conservation.

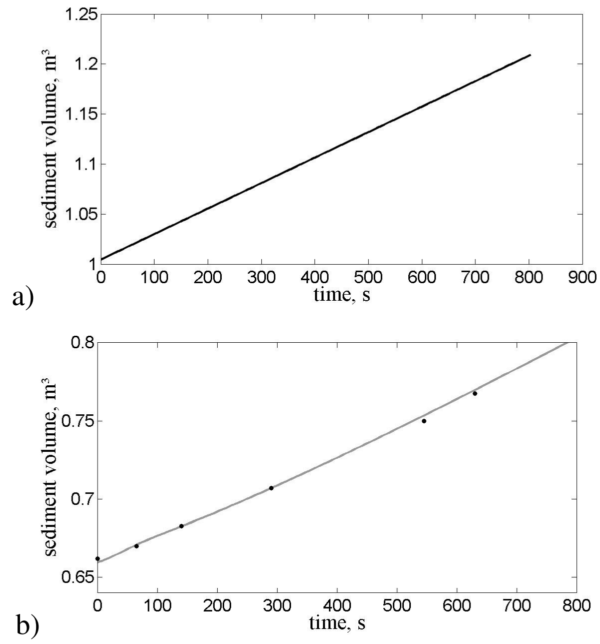

Figure 7.37. Sediment volume conservation in m³ for a unit width
— sediment supply, — numerical, • experiment

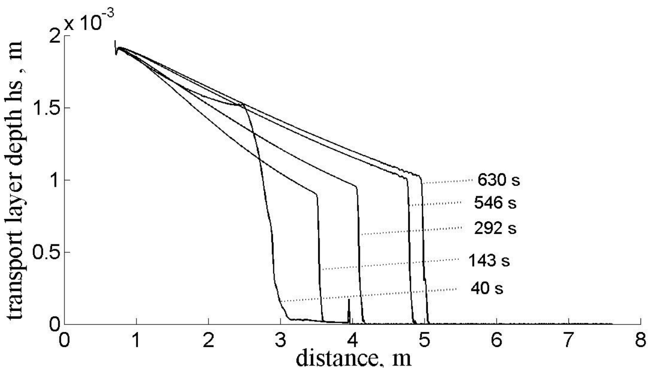

Figure 7.38. Transport layer thickness h_s (numerical results)

The computed solid discharge along the flume is plotted in Figure 7.39 for several computational times. The evolution in space and time is closely linked to the evolution of the transport layer depth (Fig.7.38). During the front propagation, the solid discharge decreases from upstream to downstream, in correlation to the development of the front thickness. This thickening progressively slows down with the decrease of solid discharge gradient. That means that an increasing part of sediment supply now contributes to the progression of the front. There is a sharp decrease of sediment discharge at the entrance due to the local deposition forming a sediment bump under the feeder.

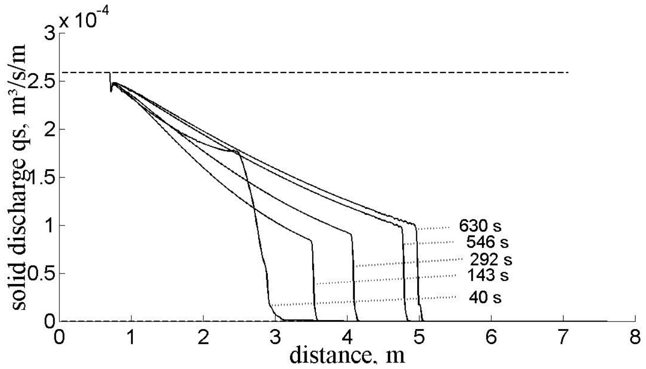

Figure 7.39. Solid discharge q_s (numerical results)

The ratio between the velocity in the transport layer and the velocity of water is plotted in Figure 7.40. This ratio is equal to zero when the transport layer depth is equal to zero. Except at the entrance and at the front, the velocity ratio is quite constant ($u_s / u_w \approx 0.22$) in space even if this constant value is slightly increasing with time. Some fluctuations of the velocity ratio at the sediment front location can also be observed. For computational times lower than 300 s, there is an area, at the toe of the sediment front, where a small transport layer thickness remains (distance < 4 m) (Fig.7.37). These areas correspond to a non-zero, but slightly smaller velocity ratio.

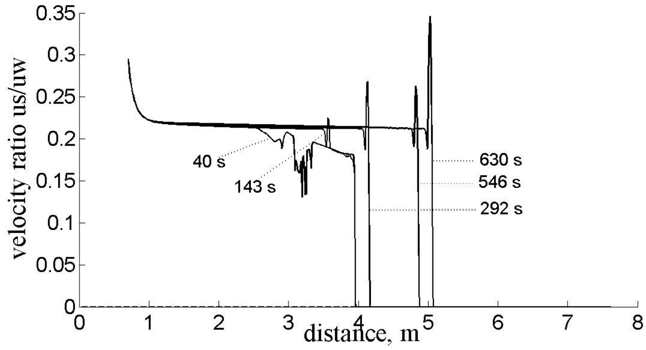

Figure 7.40. Velocity ratio u_s / u_w (numerical results)

The shear stress applied on the bed τ_s and the shear stress resisting to the flow τ_b are plotted for time t = 546 s (Fig. 7.41). In the initial condition, τ_s is greater than τ_b and, according to (2.35), erosion occurs. But, during the front propagation, e.g. at time 546 s, τ_b is greater than τ_s and there is a deposition everywhere. Indeed, if h_s is greater than the fixed threshold value, the shear stress applied to the bed is computed from (2.81): $\tau_s = \rho_s' C_{f,s} |u_s| u_s$, else, the transport layer is not considered and the shear stress applied to the bed depends on the water velocity (2.80): $\tau_s = \tau_{ws} = \rho_w C_{f,w} |u_w| u_w$.

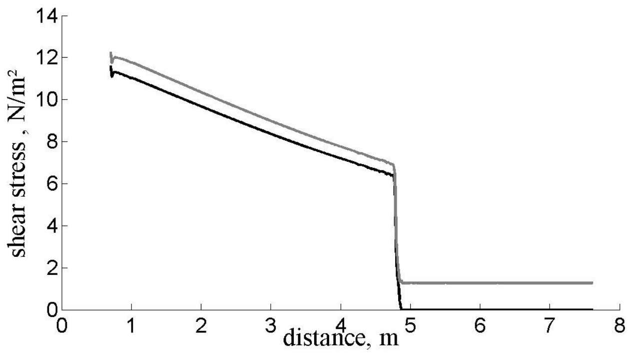

Figure 7.41. Shear stresses (numerical results), t = 546 s ▬ τ_s, ▬ τ_b

The eigenvalues along the channel are represented in Figure 7.42. In the upstream reach (supercritical flow), the four non-zero eigenvalues are positive and two of them are conjugate complex with an identical real part. In the downstream reach, the flow being subcritical, one eigenvalue becomes negative. The two intermediate eigenvalues vanish (equal to zero), when the flow is free of sediment, downstream of the front.

As previously explained, if the velocity ratio between the two layers is imposed, all the eigenvalues become real. In that case, three eigenvalues instead of four are positive upstream and the boundary condition imposing the transport layer depth is removed. The results are close with both models.

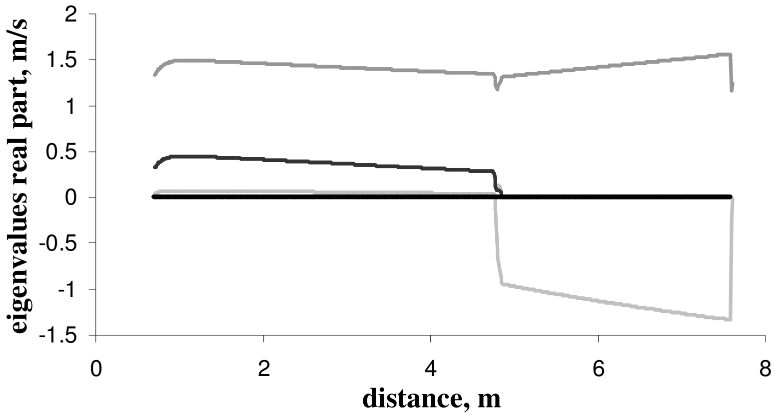

a)

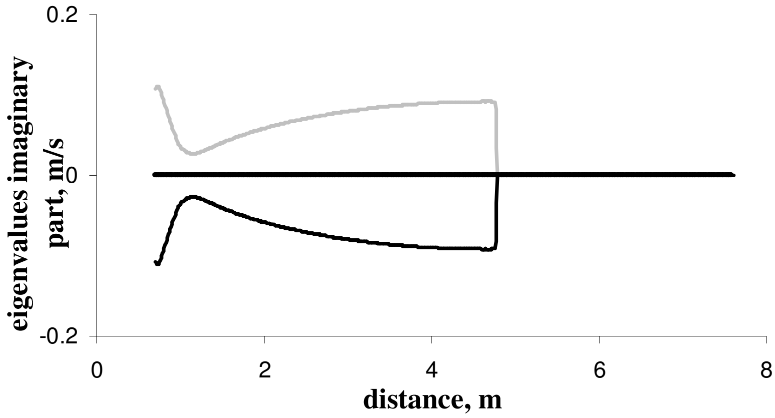

b)

Figure 7.42. Eigenvalues (numerical results) (a) real part (b) imaginary part, t = 546 s

7.3.2.2. Influence of the assumption on the sediment concentration in the transport layer

The numerical results in the above section are obtained under the assumption of similar sediment concentration in the transport layer and in the bed ($C_s = C_b = 0.57$). In the present section, the behaviour of the model is tested when the sediment concentration in the transport layer is allowed to be lower than in the bed. In this case, under deposition conditions, as exposed in sections 3.2.2.2 and 3.2.2.3 of chapter 3, a special attention has to be given to the geomorphic operator of the source treatment. Two methods are proposed to treat the geomorphic source terms when there is a deposition.

- One is exposed in chapter 3 section 3.2.2.3: the loss of energy due to the geomorphic operator, under this formulation, is not ensured (see condition 3.73 in chapter 3, section 3.2.2.2), which may lead to numerical instabilities.

- The other is proposed by Spinewine (2005): this formulation of the geomorphic operator ensures a loss of energy, but is based on the assumption equalling the shear stresses on both sides of the interface between the water and the transport layer $\tau_{sw} = \tau_{ws}$, which is wrong when this interface is moving ($e_s \neq 0$) (see (2.39) in chapter 2).

The hydraulic jump over a mobile bed, due to the deposition process occurring all along the channel and during the whole experiment, is a good test case to check if these formulations are appropriate or not. Computations will then be made with a lower sediment concentration in the transport layer $C_s = 0.4$ (while $C_b = 0.57$). As the concentration changes, the friction coefficients, still calibrated on the same basis, are modified to become $C_{f,w} = 0.015$, $C_{f,s} = 0.13$. The bed and water profiles computed with both formulations are compared together and with the experiment in Figure 7.43.

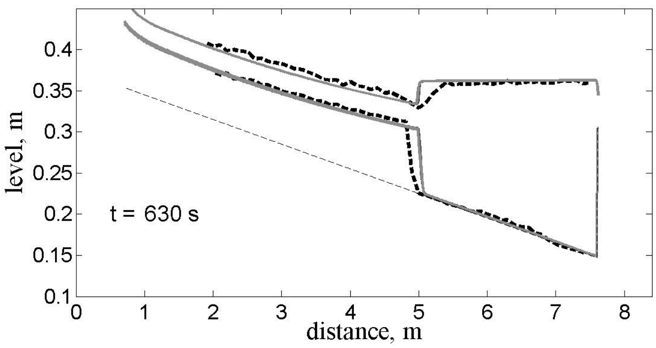

Figure 7.43. Sediment front propagation (numerical and experimental results) t = 630 s - - - initial bed, two-layer (C_s = 0.4) source operator from Spinewine (2005), two-layer (C_s = 0.4) source operator from section 3.2.2.3, ▪▪▪▪ experiment

No substantial difference appears between the two calculations. The profiles corresponding to a sediment concentration in the transport layer $C_s = C_b = 0.57$ are added (in red) in Figure 7.44. Once again, the conclusion reached is a good correspondence between the different computations. The change in concentration does not induce noticeable modifications on the numerical results, except the depth of the transport layer, which changes with the concentration. Very slight differences between the calculations appear at the sediment front location (see Fig. 7.44b, which is a zoom of Fig. 7.44a, at time $t = 630$ s).

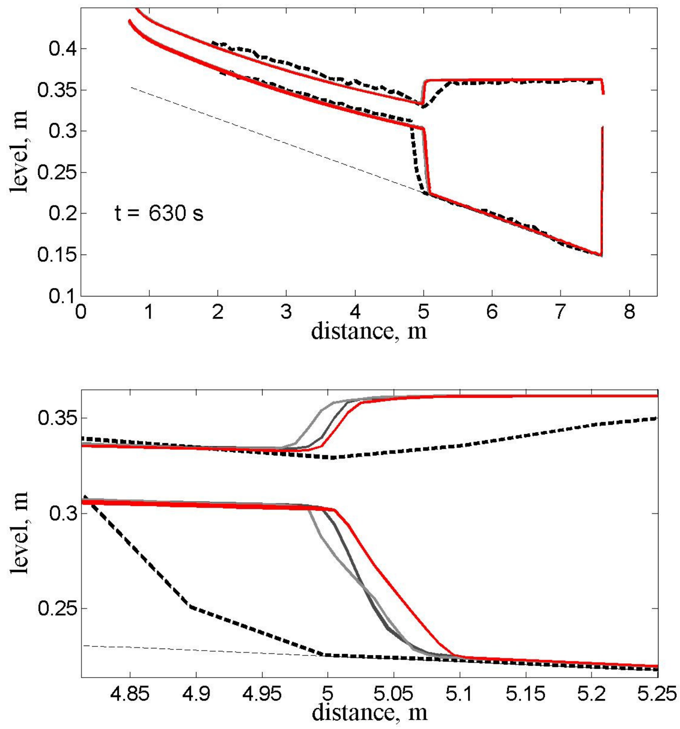

a)

b)

Figure 7.44. Sediment front propagation (numerical and experimental results) t = 630 s

- - - initial bed, two-layer ($C_s = C_b = 0.57$), two-layer ($C_s = 0.4$) source operator from Spinewine (2005), two-layer ($C_s = 0.4$) source operator from section 3.2.2.3, ▪▪▪▪ experiment

For both computations, the mass conservation (similar to Fig.7.37) is confirmed. Nevertheless, if the concentration in the transport layer C_s is imposed lower than 0.3, numerical instabilities appear (Fig.7.45). These perturbations are not dependent on the source operator chosen for the calculation, they are present in both cases.

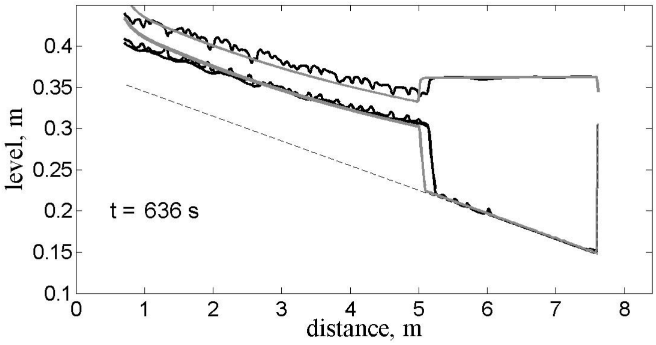

Figure 7.45. Sediment front propagation (numerical results) t = 630 s
--- initial bed, — two-layer ($C_s = C_b = 0.57$), — two-layer ($C_s = 0.22$)

7.3.2.3. Comparison with Saint-Venant – Exner

The numerical results from the two-layer model are compared (Fig. 7.46) with some results issued from a Saint-Venant−Exner approach developed by Goutière and Laraichi (2006). As exposed previously in section 4.2 of chapter 4, for the Saint-Venant−Exner model, only two boundary conditions have to be imposed at the upstream end. As the flow is supercritical upstream, the water level and the water discharge are those boundary conditions. It is thus not possible to impose in addition the sediment discharge as boundary condition, although this is fixed in the reality. Moreover q_s does not pertain to the main variables. The only solution to circumvent this problem is thus to enforce the value of q_s in the upstream cell, even if this value is not in accordance to the equilibrium one issued from the Meyer-Peter–Müller equation. Thus, contrarily to the two-layer model, where the link between q_s and the other variables may be expressed by the characteristics, this link cannot be expressed in the Saint-Venant−Exner model.

This could partly explain why the upstream reach is distinct for the two models. Moreover, the sediment transport, computed in equilibrium conditions in the Saint-Venant−Exner approach, is overestimated, leading to a faster progression of the sediment front. In contrast, the two-layer model is able to adapt the sediment discharge to the evolution of the shear stresses.

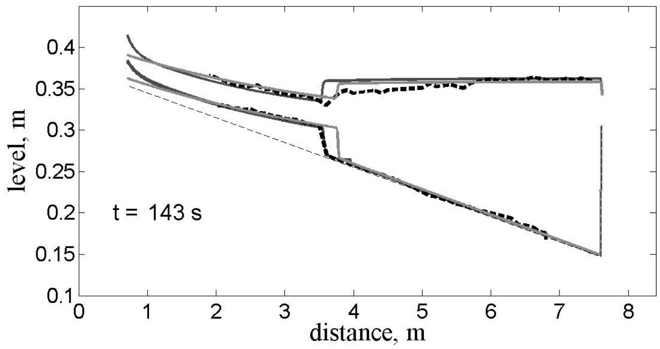

a)

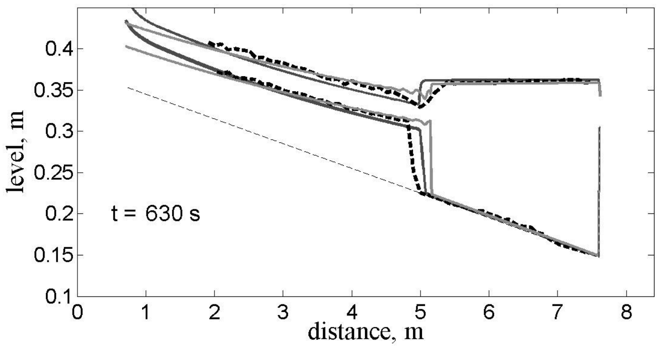

b)

Figure 7.46. Second stage sediment front propagation (numerical and experimental results) - - - initial bed, two-layer ($C_s = C_b = 0.57$), Saint-Venant−Exner, ▪▪▪▪ experiment

Moreover some spurious oscillations are generated by the Saint-Venant – Exner approach, near the front (Fig. 7.46b). The computation of the solid discharge by a closure relation (Fig.7.47) seems less stable than the one resulting from the two-layer model (Fig.7.39).

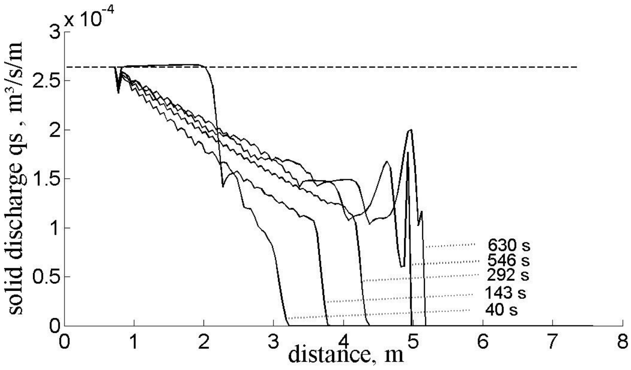

Figure 7.47. Solid discharge q_s (Saint-Venant – Exner numerical results)

In order to reduce the oscillations, the expression of the sediment flux (7.6) is modified (Goutière et al, submitted). Contrarily to (7.6), where the solid discharge (sediment flux) at the interface $i + ½$ is the mean between the solid discharge in the neighbouring cells, this discharge results now from a pondered sum taking into account the intermediate characteristic (S*), mainly linked to sediments (see eigenvectors in chapter 2, section 2.2.2). Moreover a diffusion part, taking into account the difference between the local slope $\Delta z_{b,loc}$ and the equilibrium slope $\Delta z_{b,eq}$, can be added in the expression of the flux in order to smooth discontinuities.

$$q_s^* = \frac{S^* q_{s,L} - S_L q_{s,R} + S_L S^* \operatorname{sign}(\Delta z_{b,loc})(\Delta z_{b,loc} - \Delta z_{b,eq})}{S^* - S_L} \quad (7.7)$$

This experiment was also reproduced with another numerical model (Leopardi, 2001) based on the Saint-Venant – Exner equations and using the MacCormak numerical resolution (Bellal et al., 2005), but in that case, additional instabilities occur and the results are less convincing.

7.4. Conclusions

Concerning the knickpoint migration, the results are similar for all models, there is no significant difference between the two-layer approach and the Saint-Venant – Exner model.

For the hydraulic jump, which is more challenging to model, there are more variations in the results depending on the model used. The Saint-Venant – Exner model gives quite good results, but the upstream boundary condition remains problematic as the only possibility to impose the solid discharge upstream is to introduce it in the first cell, without taking the characteristics into account. Moreover, small oscillations appear at the sediment front. These oscillations remain stable because they are damped due to a diffusive term appearing in the sediment flux calculation.

The two-layer model gives better results, without any instability, even if the internal eigenvalues are complex. The good behaviour of the two-layer model is confirmed by the mass conservation. The two geomorphic source operators in case of deposition are tested and few differences are detected. Allowing a distinct concentration between the transport layer and the bed does not change a lot the numerical results for such kind of flow. Nevertheless, instabilities may appear when the concentration in the transport layer is too low. These instabilities are not linked to the fact that the internal eigenvalues are complex